Report # DOE-OO-23917
Title: Mid-IR UAV-based sensing platform with deep learning to Identify and Quantify Gaseous Emission in Gas Flares

Final Technical Report

a. DOE Topic/Subtopic: **C56-27/a**

b. The DOE Award Number (as it appears on the award face page): **DE-SC0023917**

c. Recipient Name (as it appears on the award face page): **Omega Optics, Inc.**

d. Project Title: **Mid-IR UAV-based sensing platform with deep learning to Identify and Quantify Gaseous Emission in Gas Flares**

e. PD/PI Name, Title and Contact Information (e-mail address and phone number)

Name: Dr. Jason Midkiff,
Position: Research scientist at Omega Optics Inc.
Email: jason.midkiff@omegaoptics.com
Phone Number: (512) 996-8833 ×302

f. Project Period (Start Date, End Date): **July 10th 2023 to July 9th 2024**

g. Report Submission Date: **July 23, 2024**

h. Reporting Period Start and End Date: **July 10th 2023 to July 9th 2024**

Contents

1 Phase-I project goals and Objectives:

The broad research objective proposed in the DOE program is to develop a portable lab-on-chip mid-IR gas detection system and integrate it on a small mobile platform, such as unmanned air vehicles (UAVs) and other airborne systems or stationary locations, for routine measurement.

In Phase I of the DOE proposal, we designed an on-chip sensing waveguide, developed a platform for an adaptive sampling approach, and prepared a framework for AI/ML-based training for the overall feasibility of an integrated sensing platform.

The key objectives of this study are as follows:

1. Development of a highly sensitive and portable lab-on-chip mid-IR gas absorption device for the in situ detection of CH_4 and NO_2 with a targeted sensitivity in the ppb range. With this objective, a combustion-efficiency-level understanding of gas flare emission can be achieved. Furthermore, highly accurate and dense data can be generated to develop emission models and inventories.

2. Implementation of an adaptive sampling approach for automated UAV motion planning (i.e., one or more coordinated airborne platforms carrying the proposed sensing system) to accumulate dense sampling data from desired locations. Through this approach, we can deploy our proposed chip-based sensor for observation near to the gas flare area, which will enable us to detect incomplete combustion during flaring operations with an autonomous mode of operation.

3. Development of an AI/ML-based training approach to enhance our understanding of the combustion efficiency of internal/external variables and help identify better strategies for mitigating methane and other gas emissions.

2 Performance Evaluation: Assessing Project Accomplishments Against Established Goals and Objectives

Table 1 provides an overview of the tasks completed during Phase I and their corresponding achievements.

First, the design and fabrication of a Mid-IR Slotted Photonic Crystal Waveguide in a silicon platform were successfully accomplished, optimizing the device for detecting methane and nitrogen dioxide. Subsequently, measurements of photonic crystal waveguides were conducted, confirming the successful testing of their optical characteristics. Moreover, the gas sensing performance of the integrated photonic crystal waveguides was experimentally evaluated and shown to achieve record performance for an on-chip device. In addition, a comprehensive drone-based system for real-time gas detection was developed by integrating the critical hardware components and implementing an adaptive sampling algorithm. Initial testing using a commercially available CO_2 sensor was conducted with plans to replace it with a more sensitive and selective sensor developed in-house. Looking ahead, deep learning analysis using an optical neural network will be performed once the data collection is completed. Finally, a Phase II plan was formulated based on the outcomes and insights gained during the Phase I tasks.

Table 1: Phase-I Tasks and Results

Phase-I Tasks	Result
1. Design, and Fabrication of Mid-IR Photonic Crystal Waveguide in Silicon Platform	**The device is optimized and fabricated successfully for methane and nitrogen dioxide.**
2. Measurements of photonic crystal waveguides	**The optical characteristics of fabricated devices is successfully tested**
3. Design, Fabrication, and Characterization of polarization rotator in silicon on sapphire	**We plan to adapt ICL lasing technology with photonic wire-bonding techniques. It eliminates the need for any additional polarization rotator and makes the on-chip device more compact and easy to package.**
4. Experimentally demonstrate gas sensing performance in integrated slotted photonic crystal waveguides with TM/TE polarization rotator	**Device has been successfully tested and we detected methane and nitrogen dioxide with 3 ppm and 220 ppb detection limits. This sensitivity level is sufficient for methane measurement in the oil and gas flare.**
5. Development, testing, and validation of adaptive sampling algorithms	**We have achieved the development of a comprehensive drone-based system for real-time gas detection. Key components include a user interface, a physical drone environment, and a microcontroller network. We've integrated critical hardware components and designed an automated drone operation system. We've implemented an adaptive sampling algorithm and sophisticated user interface for real-time data visualization and analysis.**
6. Measurement analysis and analyze experimental data and compare with design	**Initial drone-based sensing testing has been done with commercially available CO_2 sensors. This commercial sensor will be replaced by our package for highly sensitive and selective measurement.**
7. Deep learning analysis of optical neural network	**After the data-collection deep learning analysis will be performed using the in-house optical neural network.**
8. Development of Phase II Plan	Completed

3 Detailed description of Phase I Research and Technical progress

3.1.1 *Task 1: Design, optimization, and fabrication of defect-based slow-light assisted waveguide photonic crystal waveguide*

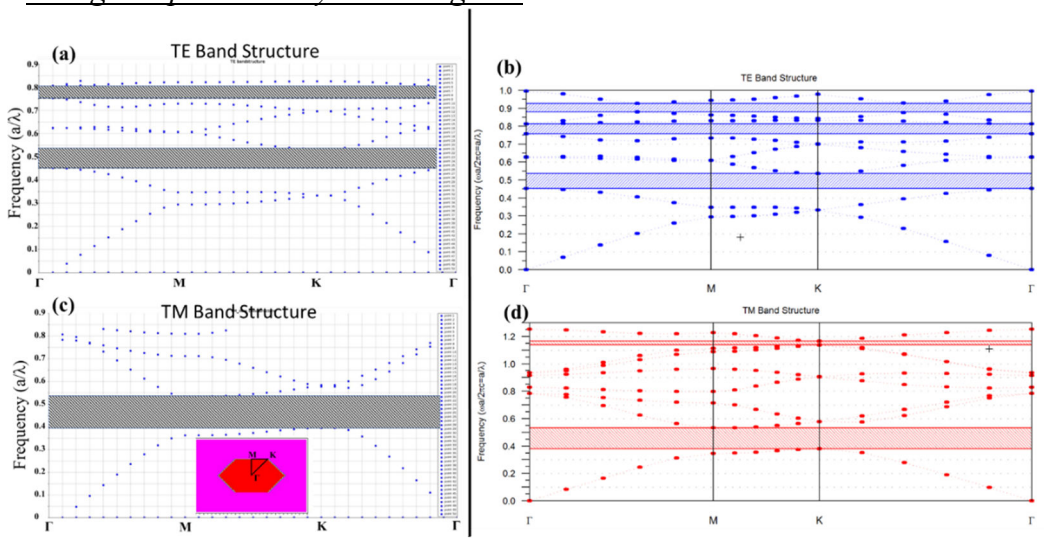

Figure 1 Comparative analysis of band structure calculations using FDTD (fig. a and c) and PWE simulation (fig. b and d) by assuming air holes in the high dielectric material of 3.42 refractive index. Band structure analysis is shown in fig. (a) and (b) are calculated for the TE band whereas fig. (c) and (d) are simulated for TM bands.

To design and optimize the 2D hexagonal structures, we performed band-structure calculations, as illustrated in Figure 1. The band structure analysis shown in Figure 1 (a) and 1(b) was calculated for the TE band, while Figure 1 (c) and 1(d) were simulated for the TM bands. We employed the Plane Wave Expansion (PWE) simulation method and the Finite Difference Time Domain (FDTD) method to extract the dispersion relation of the hexagonal air hole lattice in the silicon platform, which has a refractive index of 3.42 and similar dimensions without a central defect air hole. It is worth noting that the two analyses conducted using different methods agree well for both the TE and TM cases (Yue An, 2023):

We initially calculated in-plane dispersion relations, scanning wavevectors between Γ-M-K-Γ for various normalized frequencies to determine eigenmode solutions. In Figure 1, the solid red lines represent transverse magnetic (TM) bands, while the solid blue lines represent transverse electric (TE) bands, with the cross-hatched regions indicating bandgaps. These dispersion diagrams reveal notable band gaps for both the TE and TM polarizations. The dispersion calculations on the left side of the diagrams were derived using the Plane Wave Expansion (PWE) method, whereas those on the right side were obtained using the Finite-

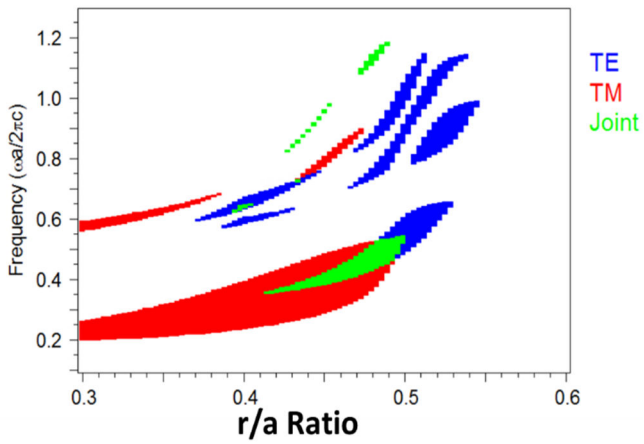

Figure 2 Bandgap analysis for different r/a ratio in hexagonal air hole lattice engraved in silicon substrate.

Difference Time-Domain (FDTD) method. Figure 2 depicts the dispersion analysis simulated through the PWE for a hexagonal air-hole lattice, employing varying radius-to-period ratios. This depiction is highly beneficial for selecting the desired regions of band gaps and determining the bandwidth within the band rejection area, all within a single diagram, and across different parameter dimensions.

When calculating the band gap dispersion diagram in a PCWs, it is also important to consider the bottom cladding, as it establishes crucial boundary conditions for the propagating modes within the waveguide. The presence of the bottom cladding defines the environment in which the waveguide operates, and significantly influences the propagation characteristics of the guided modes. Moreover, the bottom cladding plays a key role in confining light within the waveguide structure and determining the effective refractive index of the guided modes, thereby impacting the band structure and dispersion diagram of the waveguide. Additionally, interactions between the guided modes in the photonic crystal waveguide and the modes supported by the bottom cladding can lead to important mode-coupling effects. We included the bottom cladding considering two different materials: SiO_2 (Figure 3(a)) and Al_2O_3 (Figure 3(b)). Figure 3 illustrates the separation of modes based on the central plane of the Si slab, defining even parity (in red) and odd parity (in blue) within the light cone of the refractive index of the cladding. This figure distinctly outlines the bandgap region, which is crucial for designing a defect region that achieves a flat band to facilitate slow mode in the waveguide. Given our emphasis on enhancing the light-analyte interaction, we introduced and optimized the central defect waveguide using the band structure from the plane wave expansion method and optimized it through particle swarm analysis via the FDTD method.

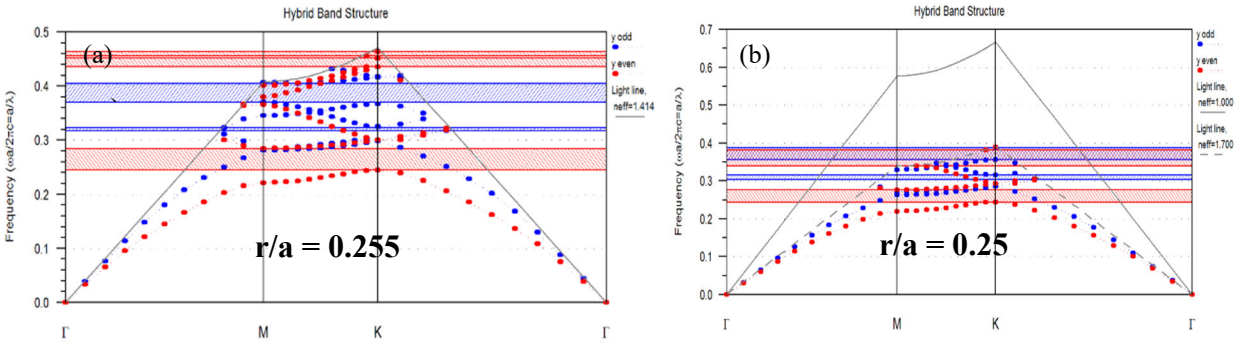

Figure 3 The computed band diagram for hexagonal arranged air holes in silicon slab with (a) bottom SiO_2 cladding, and (b) bottom sapphire cladding (Sourabh Jain, 2024).

After calculating the dispersion characteristics and observing the bandgap location, we introduced a defect region to allow the desired mode to propagate in the waveguide with the slow-light feature. This analysis parallels previous investigations conducted and documented in several previous studies. (Lai W.-C. a., 2013). Figure 4 shows the defect-based hexagonal waveguide design on an SOI-based platform. Figure 4(a) shows the centrally defined defect waveguide where regular holes (with radius "*r*") have been replaced with the smaller radius (r_s). Figure 4(b) shows the calculated detection mode location with the calculated bandgap, and Figure 4(c) illustrates the electric-field distribution of the defect mode around λ=3.4μm. The calculated group index for the defect mode was 73. It can be seen that the propagating mode is tightly bound in the defect region under a flattened dispersion regime, which results in the slow-light characteristics required for chip-scale miniaturization.

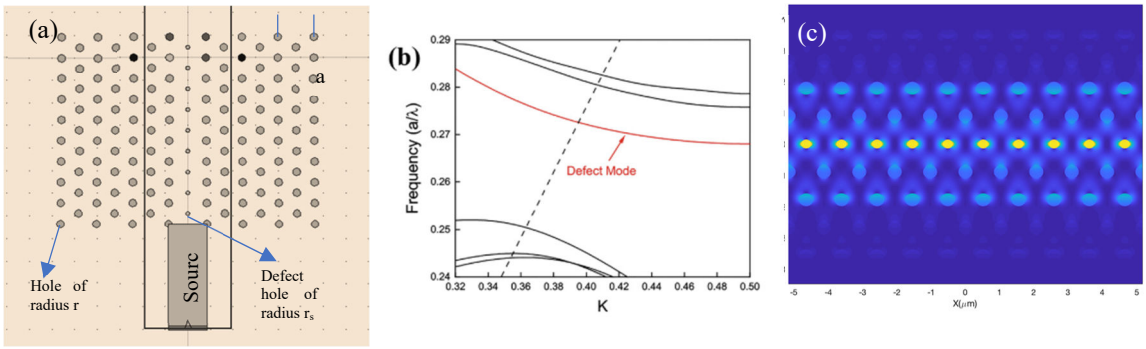

Figure 4 (a) Hexagonal photonic crystal waveguide with centrally defined defect region (rs = 0.7r). (b) calculated defect mode operating within the calculated bandgap region for h-PCW. (c) defect mode guided within the smaller holes.

3.1.2 Task 2: Design and optimization of the grating coupler for the input-output coupling

Given the nonpolarization-maintaining nature of mid-IR optical fibers, we addressed this limitation by developing polarization-selective grating couplers. These couplers effectively demonstrated the polarization rotation function at the operating wavelength. By employing these specialized couplers, we efficiently filtered the desired polarization at both the input and output stages of the optical system.

To achieve an optimal performance, we meticulously optimized the parameters of the subwavelength structure. This optimization process involved calculating critical parameters such as the air trench width, length, and period. We used an effective index approximation method for this calculation. This rigorous optimization ensures precise alignment and functioning of the grating couplers, thereby enhancing the overall efficiency and effectiveness of the optical system. Figure 5 shows the design and optimization of the grating coupler used to couple the optical signals in and out between the optical fiber and sensor chip. Figure 5(b-c) and Figure 5(d-e) represent the TE- and TM-polarized optical characteristics at λ=3.4μm respectively. Figure 5(c and e) summarize our optimized design for TE- and TM-polarization-selective subwavelength grating couplers with 25:1 and 43:1 polarization selectivities, respectively, for the respective incident angles. In addition, we modeled the 3-dB bandwidth of the coupler as approximately 500 nm. This result is encouraging, as it accommodates nano-level fabrication tolerances, ensuring consistent and reliable performance.

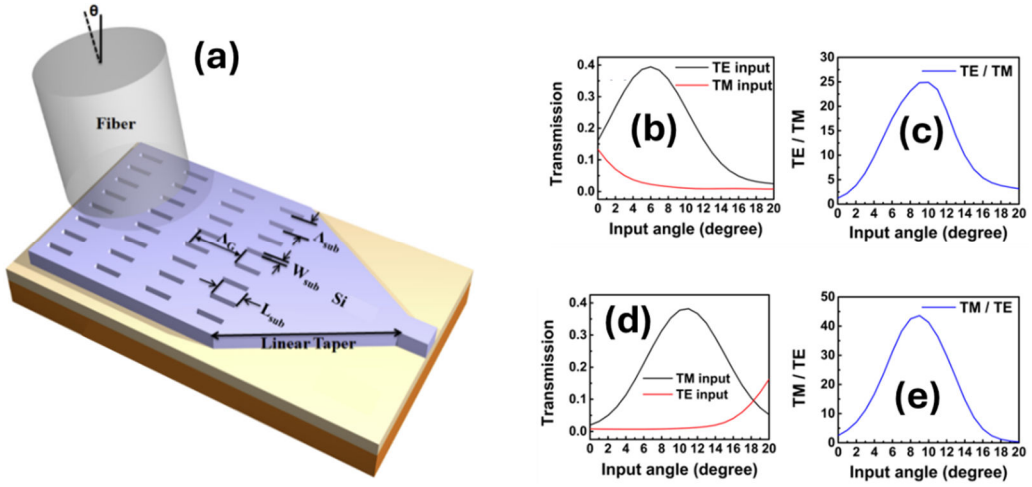

Figure 5 (a) 3D schematic of the subwavelength grating coupler. (b) and (d) Optimized optical transmission at various input angles for the TE and TM inputs, respectively. (c) and (e) illustrate the ratios between the different polarizations at the transmission port.

3.1.3 *Task 3: Fabrication of grating coupler and photonic crystal*

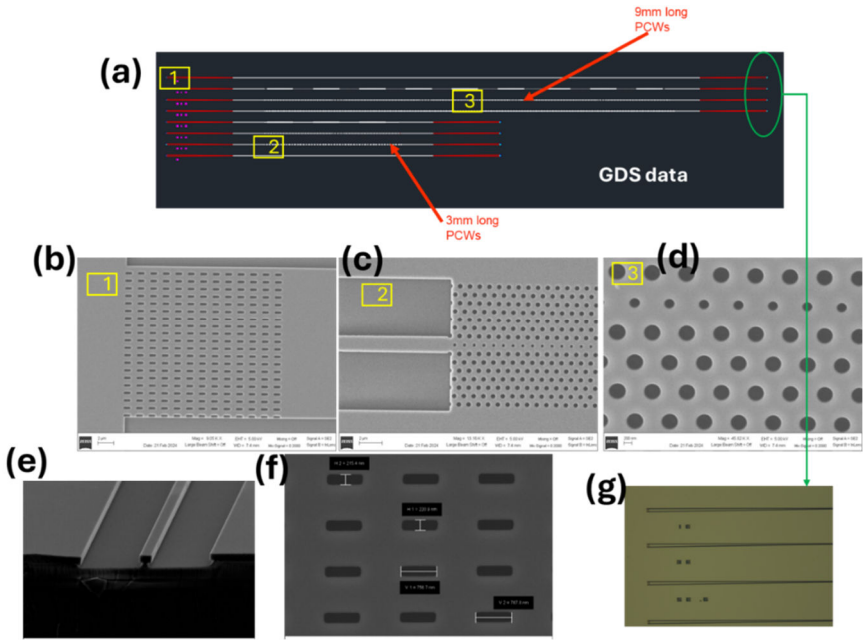

Figure 6 (a) shows the representation extracted from the GDS file for the pattern transfer to the lithography system. The three yellow boxes highlight distinct segments of the photonic structure: the grating coupler, photonic crystal waveguide, and their interconnections. The corresponding top-view SEM images of each box are shown in Figures (b). (e) Cross-sectional depiction of the strip waveguide post-dicing. (f) Dimensional measurements of the grating coupler obtained from the fabricated device. (g) Optical image depicting grating coupler section.

In Figure 6(a), according to the optimized parameters, we designed two sets of waveguides with lengths of 3 and 9 mm. Each set comprises designs featuring different structures, including grating couplers with strips, grating couplers with photonic crystal waveguides (PCWs), and grating couplers with periodically arranged PCWs. The PCW devices were fabricated on a silicon-on-insulator (SOI) wafer, featuring a 500 nm thick device layer atop a 3 μm thick buried oxide

(BOX) layer. The passive waveguide pattern was transferred to the silicon device layer using electron beam lithography and inductively coupled plasma etching techniques. Initially, a 200 nm silicon dioxide layer was deposited onto the silicon layer using plasma-enhanced chemical vapor deposition, which served as a robust mask for pattern transfer. All components underwent a unified patterning step using the JEOL JBX-6000FS electron-beam lithography tool with a ZEP-520A e-beam resist, followed by a 2-minute development in n-Amyl acetate (ZEP-N50) and rinsing in isopropyl alcohol. Subsequently, the e-beam resist pattern was translated to silicon dioxide through reactive ion etching employing CHF_3 and O_2 at a 400 V DC bias and 40 mTorr. This pattern was further transferred to silicon via inductively coupled plasma (ICP) etching, utilizing HBr and Cl_2 at 400 W ICP power, 200 W RF power, 10 mTorr pressure, and 20 Torr helium flow for backside cooling. Finally, the chip was cleaned with piranha solution, followed by three cycles of piranha/HF treatment. Figure 6(b-g) show various SEM and optical images of the fabricated devices that were tested in our measurement setup.

3.1.4 Task 4: Experimental setup and measurement analysis

Experimental Setup: Figure 7 presents a schematic overview of the gas-sensing measurement setup utilized in this study. Light emitted from a tunable pulsed laser (MIRcat-QT) undergoes collimation and is then coupled to a single-mode chalcogenide fiber using a biconvex lens. The input light, coupled into the fiber via the grating couplers, travels through the photonic crystal waveguides, and the transmitted light is subsequently extracted from the waveguide through the output gratings. Calibrated concentrations of methane and nitrogen dioxide (individually diluted in nitrogen) were introduced from a dynamic dilute system (KOFLOC) to the chip. Finally, the output signal was collected by another chalcogenide fiber and detected by an InSb detector connected to a lock-in amplifier, enhancing the signal-to-noise ratio.

Measurement: Initially, we determined the loss of the strip waveguide by creating several sets of widths and lengths on the SOI waveguide, as shown in Figure 8. In Figure 8(a), the CAD design illustrates the various lengths and widths of waveguides connected to the grating coupler. Figure 8(b) shows the optimal performance of the optical loss, which measures 1.27 dB/cm. After the initial optical testing, we conducted gas-sensing measurements for CH_4 and NO_2, as shown in Figure 9. In Figure 9 (a) and 9(b), a decrease in intensity of 5.66% and 14.94% respectively at 3.4µm and 3.42µm, is observed in the transmitted signal through the photonic crystal waveguide when CH_4 and NO_2 are activated with a flow of 25ppm concentration in N_2. (It should be noted that our existing broadband mid-IR source possesses a minimum wavelength of 3.4 µm which is used for our experiments.) Upon deactivation of the standard gas flow, the signals returned to their original levels in a pure nitrogen flow. Figure 10 shows the sensing data for a PCW exposed to different concentrations of NO_2. The absorbance values were calculated from the transmission data measured in the presence of different gas concentrations. The solid black line represents the best linear fit to the data. There are various sources of noise, including mechanical noise originating from vibrations, light source fluctuations, and the noise associated with the InSb photodiode detector. A smaller limit of detection is easily feasible by eliminating background noise. The dynamic system could provide concentrations down to 5 ppm. The limit of detection (LOD) for NO_2 of this device, calculated as three times the standard deviation (3σ), was 210 ppb. Table 2 presents a comparison and summary of the latest advancements in on-chip methane sensor performance, as demonstrated through experiments utilizing diverse technologies on various material platforms.

Table 2: Comparison of on-chip methane sensors

Spectroscopy type	**Platform**	**λ (μm)**	**Sensitivity/LOD**	**Analyte/Ref**
Wavelength Modulation Spectroscopy (WM	Nb_2O_5	3.3	348ppm	CH_4 (Bi, 2023)
Direct Absorption Spectroscopy (DAS)	SOI	1.67	100ppm	CH_4 (Lai W.-C. a., 2011)
Tunable laser diode absorption spectroscopy	SOI	1.65	100ppmv	CH_4 (Tombez, 2017)
DAS/WMS	Chalcogenide	3.291	155 ppm/75ppm	CH_4 (Zhao, 2022)
DAS	Chalcogenide	3.291	5.9ppm	CH_4 (Pi, 2023)
Our Experiments	SOI	3.3*/3.42	3.65ppm/220ppb	CH_4/NO_2

*Following Beer Lambert's law, experimental data obtained from methane sensing at 3.4 μm was utilized to extrapolate methane absorption details to 3.3 μm.

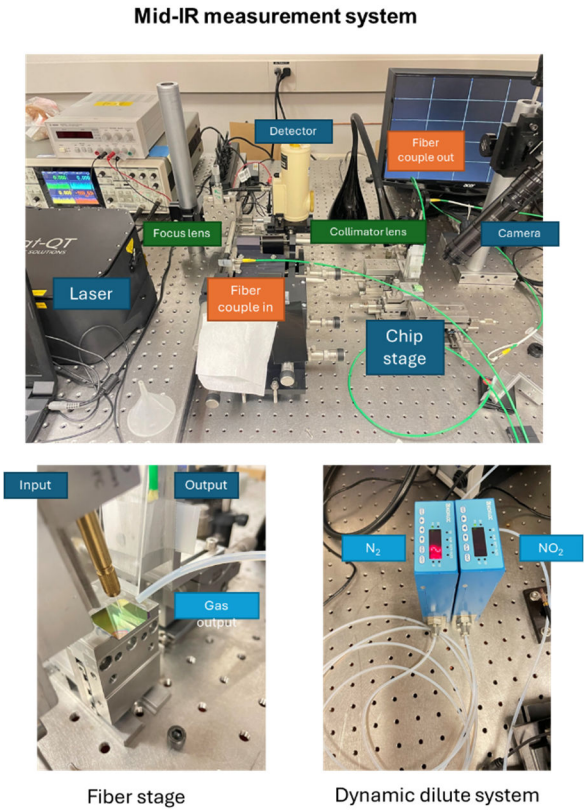

Figure 7 Photographs of the measurement system The top image presents the entire setup, encompassing a wide tunable laser (with a wavelength range of λ=3.4μm to 11μm), lens optics, detector, lock-in amplifier, and camera. In the bottom-left image, the sensor chip is aligned with the in-out grating coupler, while the bottom-right image displays a circular gas pipe connected from the dynamic dilute system

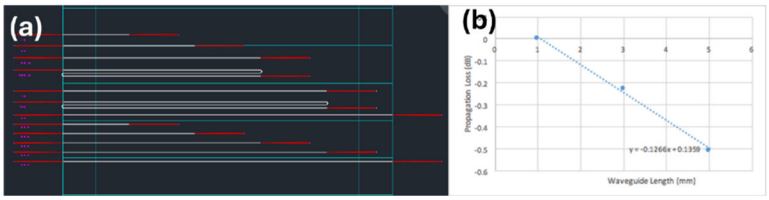

Figure 8 (a) CAD design of the various sets of optical waveguides. (b) measured optical waveguide loss normalized to the 1mm long waveguide.

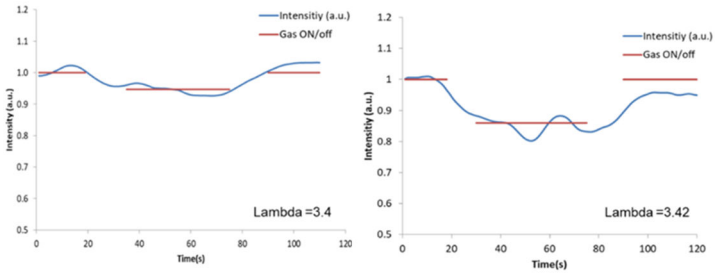

Figure 9 Measured transmitted light intensity through the 9 mm long PCW when exposed to CH_4 (left) and NO2 gas (right) diluted in N_2.

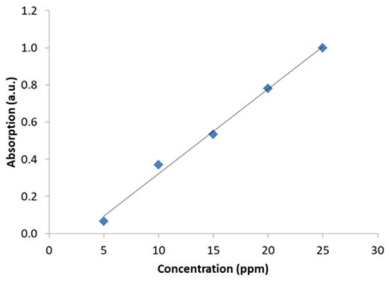

Figure 10 Sensing data for different concentrations of NO_2, blue dot is measurement data and black solid line is the best linear fit of the data.

3.1.5 Task 5: Comprehensive Drone-Based Gas Detection System with Adaptive Sampling Approach

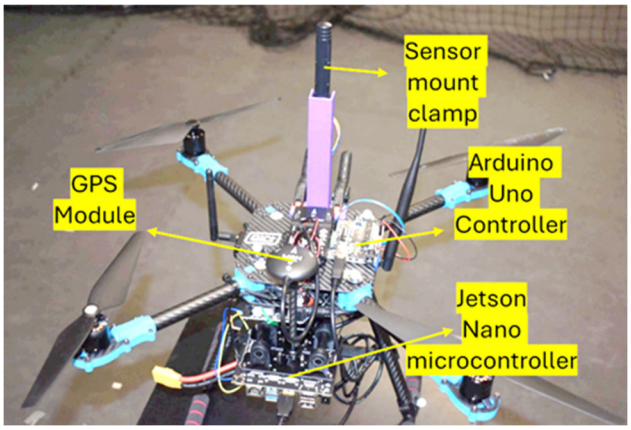

Figure 11 Real picture of drone with integrated navigation control and data transfer modules. The ground-based station (laptop) is used to automate the sampling process with adaptive sampling approach.

With the consultation and support of Dr. Maruthi Akella (serving as a consultant in Phase I), We develop a comprehensive drone-based system for detecting and monitoring gas concentrations in real-time. Our system comprises three essential components: a user interface (web application), a physical drone environment, and a microcontroller communication network. The physical drone environment involves careful hardware integration, including the mounting of critical components such as the proposed miniaturized sensor, GPS module, Jetson Nano microcontroller, and Arduino Uno controller (Figure 11). To develop an automated drone operation, data transfer, and algorithm-based operation, we initially relied on a commercially available CO_2 sensor, for which we designed a custom 3D-printed mount strategically positioned to mitigate the interference from propeller downwash during flight. Meanwhile, the microcontroller communication network enables seamless data transmission between the drone and the ground station, allowing for live monitoring and analysis of gas concentration data. This integrated approach forms a robust front-to-back end

solution for detecting environmental incidents and shows promising precise, cost-effective, and scalable gas-monitoring capabilities.

Additionally, the system incorporates an adaptive sampling algorithm using the Robot Operating System (ROS) and the integration of our GPS module and sensor data within the drone's flight model, enabling autonomous detection of the targeted gas. In our preliminary study, we aimed to detect the point source location of CO_2 gas emissions. For this purpose, our algorithm initiates data collection at predefined positions and iteratively moves the drone forward, comparing CO_2 readings at each location to identify points of the maximum concentration gradient. By systematically traversing the designated area, the drone autonomously logs the coordinates of areas with heightened CO_2 levels, thereby facilitating timely response actions. However, our Phase-I approach only considers static environmental conditions, and in the next phase of this program, we will introduce 3D wind model-based learning to enable autonomous data collection in practical dynamic environmental conditions. Furthermore, a sophisticated user interface provides real-time data visualization, signal conditioning through noise reduction using baseline correction algorithms, and intuitive interaction for sensor calibration and data denoising. The robust data storage capabilities of the interface ensure efficient organization and accessibility of sensor data, empowering users to make informed decisions based on accurate environmental insights. Together, these components and functionalities constitute a versatile and efficient system for detecting gas concentrations, addressing environmental challenges, and contributing to public health and safety.

3.1.6 Task 6: Algorithm development for spectral data analysis and graphical user interface

In this task, we developed a comprehensive software interface for visualizing and processing data from gas sensors mounted on drones. Developed using JavaScript and HTML, it incorporates a Python Baseline Correction algorithm, specifically the "Asymmetric Least Squares Smoothing" method, ensuring accurate data visualization and noise reduction. As shown in Figure 12(a), our designed interface features three main tabs: one for file uploads and processing, another for displaying interactive graphs, and a third for accessing stored data. Through rigorous testing, including real-time visualization and the evaluation of baseline correction algorithms, we confirmed the effectiveness of the interface in providing clear gas concentration representations. The adoption of the asymmetric least-squares smoothing algorithm notably improved visual displays (Figure 12(b)) despite sensor data noise, enhancing user interaction and data storage efficiency.

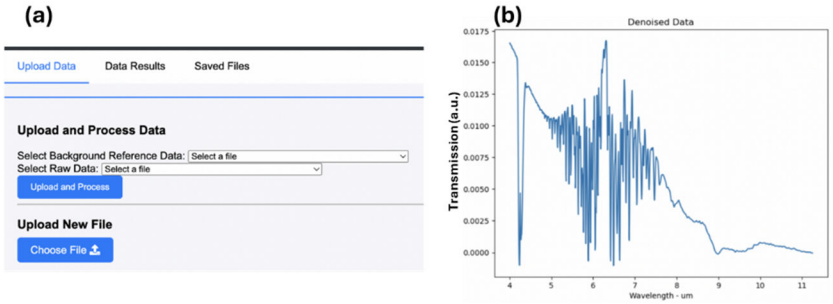

Figure 12 (a) Graphical user interface and data management for spectral analysis. (b) Denoised and baseline-corrected data using the developed Asymmetric Least Squares Smoothing Algorithm. Please note, raw data is obtained from the standard FTIR microscope.

The part of the work progress mentioned in the Task 5 and 6 can be found at (https://www.youtube.com/watch?v=JpRfepijOEs&ab_channel=RayLee)

4 Schedule Status

Proposed Milestones in Phase-I

1. **Milestone 1:** Design, and Fabrication of Mid-IR Photonic Crystal Waveguide in Silicon Platform
   Status: Completed

2. **Milestone 2:** Measurements of photonic crystal waveguides
   Status: Completed

3. **Milestone 3:** Experimentally demonstrate gas sensing performance in photonic crystal waveguides
   Status: Completed, Methane and nitrogen dioxide gas measurements at mid-IR wavelengths near $\lambda \approx 3.4\mu m$ were performed. Further developments will be performed during Phase II.

4. **Milestone 4:** Development, testing, and validation of adaptive sampling algorithms
   Status: Completed. Further development will be performed during Phase II.

5. **Milestones 5:** Measurement analysis and comparison with design
   Status: Completed.

5 Research Product

5.1 Publication

1. Sourabh Jain, May H. Hlaing, Kang-Chieh Fan, Jason Midkiff, and Ray T. Chen, "On-Chip Mid-IR Spectroscopy with Slow Light Enhanced Silicon-on-Sapphire Waveguide" JTh2A.62, CLEO-2024 (Accepted).
2. Sourabh Jain, May Hlaing, Kang Chieh Fan, Jason Midkiff, Shupeng Ning, Chenghao Feng, Po Yu Hsiao, Patrick Camp, Ray Chen, "Incubating Advances in Integrated Photonics with Emerging Sensing and Computational Capabilities", arxiv.org/abs/2403.19850, 2024.
3. We are currently writing a technical manuscript entitled "***Revolutionizing Methane Detection: Cutting-edge Mid-IR On-Chip Spectrometer Enhanced by Slow-Light Technology***."

6 Bibliography

Aldhafeeri, T. e. (2020). A review of methane gas detection sensors: Recent developments and future perspectives. *Inventions, 5*(3), 28.

Bi, R. a. (2023). A niobium pentoxide waveguide sensor for on-chip mid-infrared absorption spectroscopic methane measurement. *Sensors and Actuators B: Chemical, Elsevier, 382*, 133567.

Dey, A. (2018). Semiconductor metal oxide gas sensors: A review. *Materials science and Engineering: B, Elsevier, 229*, 206-217.

Fullager, D. B. (2017). Infrared dielectric response of nanoscribe IP-dip and IP-L monomers after polymerization from 250 cm- 1 to 6000 cm- 1. *Optical Materials Express, 7*(3), 888-894.

GASERA. (2024). https://www.gasera.fi/technology/solidphase-pas/.

Hamamatsu, "InAsSb photovoltaic detector," P16612-011CA/CN datasheet, Cat. No. KIRD1145E05, Jan. 2024. (n.d.).

Harrison, M. R. (1996). *Methane emissions from the natural gas industry.* US Environmental Protection Agency, National Risk Management Research Laboratory.

Hosseini, A. a. (2011). On the role of evanescent modes and group index tapering in slow light photonic crystal waveguide coupling efficiency. *Applied Physics Letters, 98*(3).

https://www.youtube.com/watch?v=JpRfepijOEs&ab_channel=RayLee. (n.d.).

Inc., P. S. (2024). http://www.psicorp.com/products/laser-basedsensors/gasscan.

Lackner, M. (2007). Tunable diode laser absorption spectroscopy (TDLAS) in the process industries--a review. *Reviews in Chemical Engineering, 23*(2), 65-147.

Lai, W.-C. a. (2011). On-chip methane sensing by near-IR absorption signatures in a photonic crystal slot waveguide. *Optics letters, 36*(6), 984-986.

Lai, W.-C. a. (2013). Slow light enhanced sensitivity of resonance modes in photonic crystal biosensors. *Applied physics letters, 102*(4).

Laird Thermal Systems, "Ceramic plate series thermoelectric cooler," CP10-31-08-L1-W4.5 datasheet, Jun. 2022. (n.d.).

Lindenmann, N. a. (2011). Photonic waveguide bonds--a novel concept for chip-to-chip interconnects. *Optica Publishing Group.*

Liu, W. a. (2021). Suspended silicon waveguide platform with subwavelength grating metamaterial cladding for long-wave infrared sensing applications. *Nanophotonics, 10*(7), 1861-1870.

Lu, H. a. (2020). Leakage detection techniques for oil and gas pipelines: State-of-the-art. *Tunnelling and Underground Space Technology, Elsevier, 98*, 103249.

Ma, Y. (2018). Review of recent advances in QEPAS-based trace gas sensing. *Applied Sciences, 8*(10), 1822.

MenloSystems. (2024). https://www.menlosystems.com/products/optical-frequency-combs/.

Myhre, G. D. (2023). Climate change 2013: the physical science basis. Contribution of Working Group I to the Fifth Assessment Report of the Intergovernmental Panel on Climate Change. UK: IPCC, Cambridge Univ. Press, pp. 659-740.

N. Lindenmann, ". b.-o.-i.–1. (n.d.).

N. Lindenmann, e. a.–A.-t.-c.–5. (n.d.).

Nanoplus, ". W. (n.d.).

Patil, C. M. (2022). Observation of slow light in glide-symmetric photonic-crystal waveguides. *Optics express, 30*(8), 12565-12575.

Pi, M. a. (2023). Ultra-wideband mid-infrared chalcogenide suspended nanorib waveguide gas sensors with exceptionally high external confinement factor beyond free-space. *ACS Nano, 17*(18), 17761-17770.

Plant, G. e. (2022). Inefficient and unlit natural gas flares both emit large quantities of methane. *Science, 377*(6614), 1566-1571.

Product, M. (2024). https://www.mks.com/g/products.

Riser-Roberts, E. (2020). *Remediation of petroleum contaminated soils: biological, physical, and chemical processes.* CRC press.

Rostamian, A. a.-K. (2021). Towards lab-on-chip ultrasensitive ethanol detection using photonic crystal waveguide operating in the mid-infrared. *Nanophotonics, 10*(6), 1675-1682.

Sourabh Jain, M. H.-C. (2024). On-Chip Mid-IR Spectroscopy with Slow Light Enhanced Silicon-on-Sapphire Waveguide. *CLEO.*

Tan, X. e. (2020). Non-dispersive infrared multi-gas sensing via nanoantenna integrated narrowband detectors. *Nature communications, 11*(1), 5245.

Texas Instruments, "LMP91051 configurable AFE for nondispersive infrared (NDIR) sensing applications," LMP91051 datasheet, SNAS581B, May 2013. (n.d.).

Thorpe, M. J. (2006). Broadband cavity ringdown spectroscopy for sensitive and rapid molecular detection. *Science, 311*(5767), 1595-1599.

Thorpe, M. J. (2006). Broadband cavity ringdown spectroscopy for sensitive and rapid molecular detection. *Science, 311*(5767), 1595-1599.

Tiger-optics. (2024). https://www.tigeroptics.com/products.html.

Tombez, L. a. (2017). Methane absorption spectroscopy on a silicon photonic chip. *Optica, 4*(11), 1322-1325.

Wavelength Electronics, ". P.-0. (n.d.).

Wavelength Electronics, "WTC32ND & WTC32ND-EV," WTC32ND-0400 Rev A datasheet, Jan. 2022. (n.d.).

Wu, Y. a. (2018). Optical graphene gas sensors based on microfibers: a review. *Sensors, MDPI, 18*(4), 941.

Yoo, K. M.-j. (2020). InGaAs membrane waveguide: a promising platform for monolithic integrated mid-infrared optical gas sensor. *ACS sensors, 5*(3), 861-869.

Yue An, S. J. (2023). Highly Efficient Atmospheric Gases Detections Using Slow Light Effect Induced in Vertical CrystalWaveguide Arrays. *CLEO.* San Jose.

Zhao, H. a. (2022). On-chip mid-infrared silicon-on-insulator waveguide methane sensor using two measurement schemes at 3.291μm. *Frontiers in Chemistry, 10*, 953684.

Zou, Y. a. (2014). The role of group index engineering in series-connected photonic crystal microcavities for high density sensor microarrays. *Applied physics letters, 104*(14).